RESEARCH ARTICLE

Computational fluid dynamics for the optimization of internal bioprinting parameters and mixing conditions

Gokhan Ates[1,3]*, Paulo Bartolo[1,2]*

[1]Department of Mechanical, Aerospace and Civil Engineering, The University of Manchester, Manchester, United Kingdom

[2]Singapore Centre for 3D Printing, School of Mechanical and Aerospace Engineering, Nanyang Technological University, Singapore

[3]Department of Mechanical Engineering, Abdullah Gul University, Kayseri, Turkey

*Corresponding authors:
Gokhan Ates
(gokhan.ates@manchester.ac.uk)

Paulo Bartolo
(pbartolo@ntu.edu.sg)

Abstract

Tissue engineering requires the fabrication of three-dimensional (3D) multimaterial structures in complex geometries mimicking the hierarchical structure of biological tissues. To increase the mechanical and biological integrity of the tissue engineered structures, continuous printing of multiple materials through a printing head consisting of a single nozzle is crucial. In this work, numerical analysis was carried out to investigate the extrusion process of two different shear-thinning biomaterial solutions (alginate and gelatin) inside a novel single-nozzle dispensing system consisting of cartridges and a static mixer for varying input pressures, needle geometries, and outlet diameters. Systematic analysis of the dispensing process was conducted to describe the flow rate, velocity field, pressure drop, and shear stress distribution throughout the printing head. The spatial distribution of the biopolymer solutions along the mixing chamber was quantitatively analyzed and the simulation results were validated by comparing the pressure drop values with empirical correlations. The simulation results showed that the proposed dispensing system enables to fabricate homogenous material distribution across the nozzle outlet. The predicted shear stress along the proposed printing head model is lower than the critical shear values which correspond to negligible cell damage, suggesting that the proposed dispensing system can be used to print cell-laden tissue engineering constructs.

1. Introduction

Three-dimensional (3D) bioprinting technology, within the rapidly evolving field of biomanufacturing, enables to engineer predesigned, volumetric tissue-like structures with a spatially controlled distribution of cells and biomolecules, making it a unique tool for a broad range of tissue engineering applications[1-3]. Bioinks are the bioprintable materials composed of hydrogels encapsulating cells or cell aggregates[4].

The most commonly used additive manufacturing (3D printing) techniques[5,6] to create cell-laden constructs are material jetting[7,8], extrusion-based[2,9], and light-based technologies[10,11]. Multimodal systems, integrating different printing principles into a single machine, have been also proposed[6]. Among these printing strategies, extrusion-based bioprinting is one of the most commonly used approach as it allows to print materials with a wide range of viscosities and to fabricate multimaterial/cellular volumetric biological constructs[12-14]. In extrusion bioprinting, biocompatible cell-laden hydrogels are loaded into the cartridges (reservoirs) and deposited on a bioprinting platform using one or several nozzles via pneumatic, mechanical, or solenoid actuation[5].

A key object of tissue engineering applications is the fabrication of multimaterial and multiscale heterogeneous constructs, mimicking the organized cellular architecture and functionality of natural tissues[15]. However, this is not achievable with single-material bioprinting approaches, as they often fail to replicate the complexity and variety of real tissues consisting of multiple layers of different cell types[16]. To overcome this shortcoming, multimaterial bioprinting emerged as a promising approach[6,15-17]. Multimaterial 3D bioprinting technique refers to the simultaneous or sequential deposition of two or more biomaterials in a predetermined manner to create region-specific characteristics and performances[16]. These type of heterogeneous bioconstructs have been fabricated using multireservoir and multinozzle printing systems[18]. However, the fundamental limitation of these multinozzle bioprinting systems is the considerably long printing time while switching between different bioinks, in addition to the need of accurate calibration of all printheads before the deposition process[3,19,20]. Moreover, multinozzle bioprinting systems result in a discontinuity in the printed filament morphology that adversely affect the mechanical integrity of the 3D-printed structures[19]. To overcome these limitations, several researchers focused on bioprinting of multiple hydrogels through a single nozzle[20-23].

Implementing multireservoir single-nozzle systems is simple, though this strategy is ineffective for systematically printing tissue engineering structures with continuous gradient features. A variety of mixers have been used to tackle this limitation by blending two or more biomaterials in various concentrations to facilitate multimaterial bioprinting tasks[23]. In this case, active and passive or static mixers have been extensively studied. Static mixers are usually easier to assemble and more biocompatible compared to active mixers, since they cause less shear stresses to the encapsulated cells[24]. Recently, Kenics static mixers (KSM) have been employed to enable chaotic bioprinting of multimaterial constructs[15] and this is a

rapidly expanding field to overcome the restrictions of mixing highly viscous biomaterials[25].

Computational fluids dynamics (CFD), simulations of the biopolymer flow in extrusion-based bioprinting processes, are widely used to understand the relationship between printing parameters, nozzle size and geometry, viscous forces, and material properties during the bioprinting process. More specifically, it enables to determine inner parameters that are experimentally difficult to evaluate, such as pressure, velocity, flow rate, and also shear stresses on cells in the case of bioinks. It is known that the dispensing pressure, and particularly shear stresses, have a significant influence on cell survival[26-29]. However, only few simulation studies have investigated shear stresses and cell viability on extrusion-based bioprinting processes, considering different nozzle geometries and dispensing pressures[30-34]. Moreover, all these studies have only considered the simulation of a single-material bioprinting process.

In this work, we extensively investigated the extrusion process of non-Newtonian alginate and gelatin solutions, through an entire and novel dispensing system consisting of two cartridges, KSM integrated mixing chamber and a single nozzle. To the best of our knowledge, to date, no numerical study has yet investigated the inner parameters such as shear stress, pressure, and velocity field as well as mixing index within the KSM-embedded 3D model of printing head flow domain. The spatial distribution of the two different polymer solutions was quantitatively characterized by determining the mixing index. To understand the effect of the printing needle geometry on the inner parameters, cylindrical and conical nozzles with varying outlet diameters were investigated considering different printing pressures. The simulation results were validated by comparing predicted pressure drop results at different Reynolds numbers with existing empirical correlations. This model can be easily adapted to different biomaterials.

2. Materials and methods

2.1. Computational fluid dynamics analysis

A computational fluid dynamics (CFD) analysis was performed by using the simulation software package ANSYS® Academic Research Fluent 19.2 (ANSYS, Canonsburg, PA, USA) to numerically evaluate the mixing mechanism of two different biomaterials through a static mixer integrated printing head, and both the velocity and shear stress distribution profiles at the needle outlet during the extrusion process. Figure 1 shows the computer-aided design (CAD) model of the printing head equipped with cartridges, static mixer, and a cylindrical or a conical
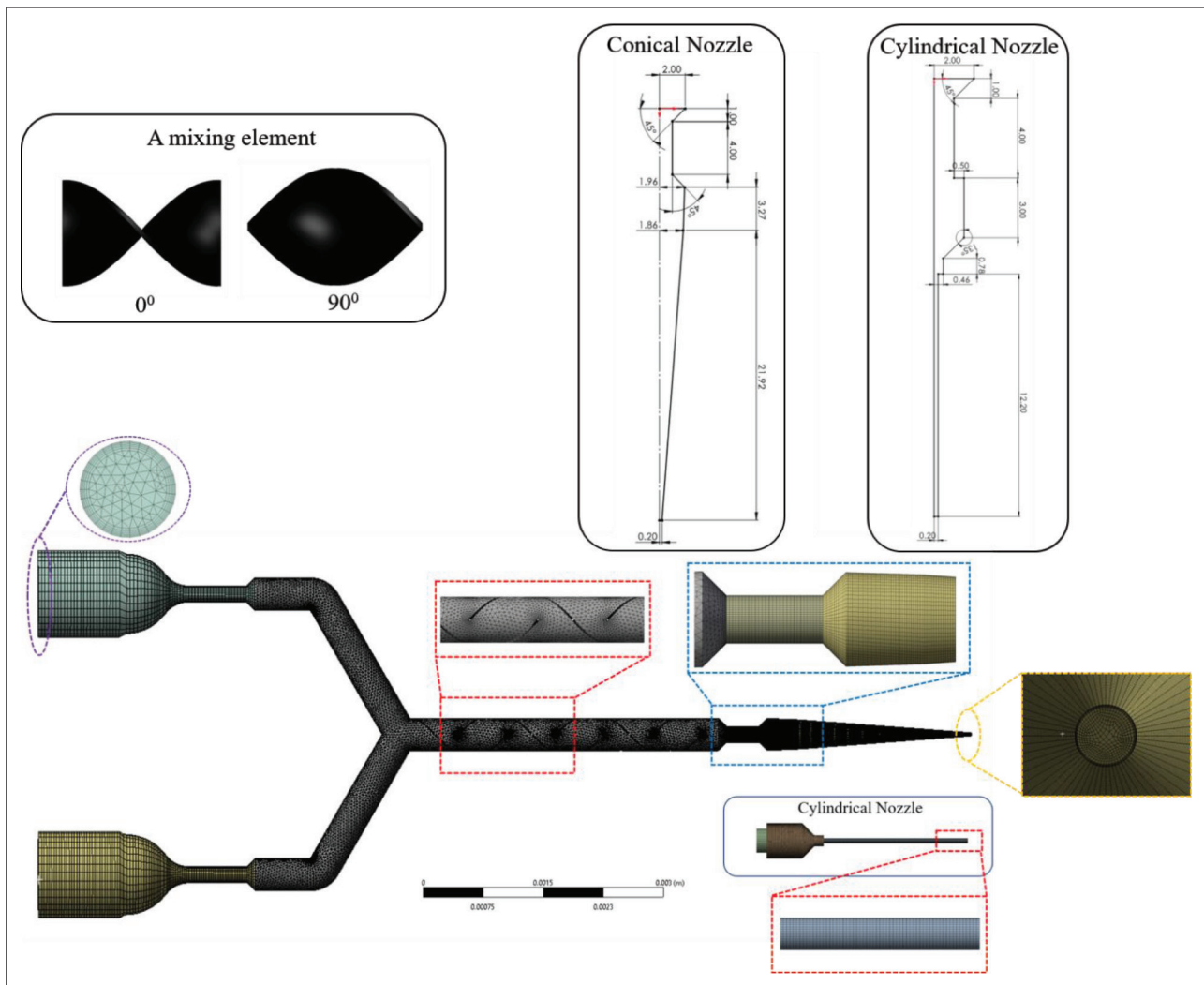
Figure 1. Representation of mesh generation on the printing head and corresponding dimensions in mm.

printing needle. In this study, a miniaturized Kenics-type static mixer[35-38], consisting of multiple helical mixing units alternating clockwise and counter-clockwise directions, was used in all simulations.

For the simulations, the material flow was assumed to be multicomponent, laminar, incompressible, isothermal, in steady state, and non-Newtonian, and have no chemical reactions occurring inside the printing head during the printing process. The volume continuity, momentum conservation, and transport equations for an incompressible flow are solved by finite volume method and given as follows[38]:

$$\nabla.(\rho u) = 0 \qquad (I)$$

$$\nabla.(\rho uu) = -\nabla P + v\nabla^2 u \qquad (II)$$

$$(u.\nabla)C = -\nabla^2 C \qquad (III)$$

where u is velocity (m/s), α is the kinematic diffusivity coefficient (m^2s^{-1}), C represents one of the mixing fluid's concentration in the KSM channel, ρ is the fluid density (kg/m^3), and P denotes the pressure (Pa).

The relationship between shear stress and apparent shear rate for a non-Newtonian fluid can be described by the following power-law model[39].

$$\tau = k\dot{\gamma}^n \qquad (IV)$$

where k is the fluid consistency index ($Pa.s^n$), and n is power-law index (dimensionless) that, depending on the material rheological behavior, assumes the following values[40]:

- $n<1$, the fluid exhibits a shear-thinning behavior
- $n=1$, the fluid exhibits a Newtonian behavior
- $n>1$, the fluid exhibits a shear-thickening behavior.

Table 1. Rheological parameters of alginate and gelatin solutions[34,42]

	Content	n	k [Pa s^n]
Alginate	0.5 w/v%	0.977	0.032
	1.0 w/v%	0.895	0.119
	1.5 w/v%	0.840	0.346
Gelatin	7.0 w/v%	0.795	0.240

Materials to be printed through pneumatic (compressed air), mechanical (piston or screw), or solenoid (electrical pulses) driven printheads must exhibit shear-thinning properties, as this behavior allows to reduce shear stresses during the printing process and to enhance cell viability. The shear rate $\dot{\gamma}(s^{-1})$ can be defined as follows:

$$\dot{\gamma} = \frac{du}{dr} = \frac{-\Delta P}{2\mu L} r \qquad (V)$$

where r (m) is the radius of the pipe, L (m). According to Metzner et al.[41], the generalized Reynolds number for a shear-thinning fluid is given by:

$$Re = \frac{\rho u^{2-n} D^n}{\dfrac{k}{8}\left(\dfrac{6n+2}{n}\right)^n} \qquad (VI)$$

where D is the pipe diameter (m).

In this study, non-crosslinked alginate and gelatin solutions were selected as the working fluids. The rheological data for both materials arepresented in Table 1.

In the simulations, all solid boundaries were considered as stationary walls, where the "nonslip" boundary condition was applied. Moreover, by adjusting the dispensing pressure at the inlet boundaries, different Reynolds numbers were obtained for the flow domain. The outlet boundary condition was set as atmospheric pressure in all simulations. The stationary solver was used to resolve the model, and calculations were carried out using pressure–velocity coupling (Coupled algorithm). To discretize the momentum and pressure formulation, a second-order upwind method was used, while the least-squares cell-based method was used for the gradients. The relaxation parameters for pressure and momentum were set as 0.5 and set to 1.0, for body forces and density, respectively. For all simulations, the relative residuals of the velocity and continuity components were less than 10^{-5}, after approximately 1000 iterations, corresponding to a reasonably short calculation time ($\leq$30 min) on an Intel processor with four cores. Convergence analysis was also tested, by monitoring the area-weighted average values of the shear stress and the velocity at the outlet. A stationary solution was achieved when these parameters reached a state of convergence.

To further investigate the effect of nozzle geometries (cylindrical and conical) and process parameters on cell viability, the flow rate, velocity magnitude, and shear stresses at the outlet, as well the axial discharge of the dispensing pressure along the printing head, were evaluated for the converged solution. A variety of nozzle outlet diameters, ranging from 0.25 to 2.00 mm, were examined at different inlet pressures (0.1–3.0 bar) for both nozzle types.

2.2. Mesh independence test

The 3D flow domain of the KSM-integrated printing heads was discretized, using the selective meshing feature of ANSYS Workbench meshing tool to create as many structured (hexahedral) elements as possible, and fill the remaining parts with tetrahedron elements. In this case, as the printing head consists of multiple bodies, we used the patch conforming method for the Y-shaped main body including the KSM, and the sweep method for sweepable bodies, such as barrels, and the other cylindrical parts (Figure 1). The mesh quality was refined near the mixing elements, and inflation layers were created for the pipe walls, to capture the flow fields more precisely in those places. To obtain reliable numerical results, grid-independence tests were conducted for all needle geometries with varying outlet diameters. These preliminary test results enabled to establish the best node layout and cell density, for numerical accuracy and computational load. Thus, a mesh sensitivity study was performed to observe how the outlet velocity magnitude deviates as the number of grids increased. The discretization of the models used in CFD simulations for both nozzle types is shown in Figure 1.

As shown in Figure 2, the calculated maximum velocity magnitude was stabilized by increasing the number of elements. Grid independence was achieved for the cylindrical and conical nozzle models, with 6×10^5 elements and 8×10^5, respectively, beyond that no substantial changes were observed. Based on these preliminary convergence test results, a mesh of 7.3×10^5 and 9.8×10^5 elements were chosen as the optimal mesh density, as it provides high accuracy of results with a shorter computational time required for convergence. The maximum skewness for all model meshes were lower than 0.85, with a minimum value of 2.3×10^{-5} and a minimum element quality of 0.09, which according to the literature is a nice evidence of good mesh quality[43].

2.3. Mixing index

The distributive capacity of the Kenics mixer was also investigated for different flow velocities. Distributive mixing, also known as simple or extensive mixing, represents the spatial distribution of the components
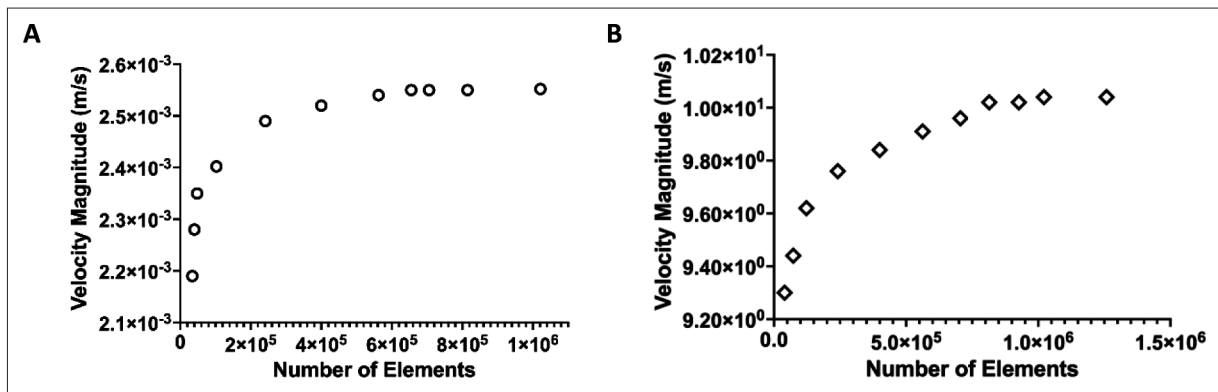
Figure 2. Mesh independence test results obtained for (A) the cylindrical and (B) the conical nozzle-integrated models.

across the fluid domain and, compared to dispersive mixing, it is easier to achieve. As the distributive mixing capacity of a mixer cannot be only judged based on the visual contour, it is essential to quantitatively evaluate the mixing performance. Therefore, the mixing efficiency of the static mixer was analyzed using a statistical measurement method based on the concept of intensity of segregation[44]. As previously reported by other studies on mixing processes[45-49], mixing can be quantified using the mixing index, denoted by M.I, at a cross-sectional plane perpendicular to the flow direction as follows:

$$M.I = 1 - \sqrt{\frac{\sigma^2}{\sigma^2_{max}}} \qquad (VII)$$

where σ^2_{max} denotes maximum possible variance at a cut-plane normal to the flow direction and σ^2 refers to the actual variance, which is defined as:

$$\sigma^2 = \frac{1}{n}\sum_{i=1}^{n}(c_i - \overline{c})^2 \qquad (VIII)$$

where c^i is the mass fraction at i^{th} sampling point, $\overline{c}$ is the optimal mixing mass fraction and n is the number of sampling points on the associated plane. The optimal mass fraction ($\overline{c}$) at the cut plane is equal to 0.5 for symmetrical boundary conditions[49]. The maximum variance (σ^2_{max}) is determined by the following equation:

$$\sigma^2_{max} = \overline{c}(1-\overline{c}) \qquad (IX)$$

As the optimal maximum mass fraction, c, is equal to 0.5, in the case of equal flow of the two fluid streams, the value of σ^2_{max} is assumed to be 0.25. The mixing index varies from 0 (representing completely unmixed state) to 1 (completely mixed fluid). As the mixing index decreases from 1 to 0, a lesser amount of mixing is achieved. Equally, the higher mixing index represents higher mixing performance. However, it has been reported that numerical results might overestimate the mixing quality, owing to numerical diffusion[50].

2.4. Model validation

The validation of the CFD simulations was conducted by evaluating the pressure drop, as it is more sensitive to numerical oscillations in comparison to velocity[51]. Thus, the pressure drop values, obtained from the numerical simulations at different Reynolds numbers, were compared with the available empirical correlations[37,52-54]. In general, these correlations for static mixers are often stated in terms of a Z-factor[37]. The Z-factor is determined by the ratio of the pressure drop within the static mixer, ΔP, to the pressure drop in the empty pipe with the same length and diameter, ΔP_0[37], as follows[54]:

$$Z = \frac{\Delta P}{\Delta P_0} \qquad (X)$$

For the laminar flow regime, the Z-factor for Kenics type mixers range between 5 and 8[44]. The pressure drop without a mixer is defined by the Hagen–Poiseuille equation[37]:

$$\Delta P_0 = \frac{32}{Re}\frac{\rho u^2 L}{D} \qquad (XI)$$

Wilkinson and Cliff[37] presented a pressure drop correlation for Kenics mixers based on the Ergun equation, which is defined as:

$$Z = 7.19 + \frac{\Delta P}{32} \qquad (XII)$$

Another commonly used equation, to estimate Z-factor in Kenics mixers, was developed by Grace[52] as follows:

$$Z = 3.24(1.5) + 0.21\sqrt{Re} \qquad (XIII)$$

Shah and Kale[53] account for the volume drop caused by the presence of KSM elements by proposing the following equation:

$$Z = \frac{1}{16\varepsilon}\left(64.06 + 1.84\left(\frac{Re}{\varepsilon}\right)^{0.66}\right) \qquad (XIV)$$
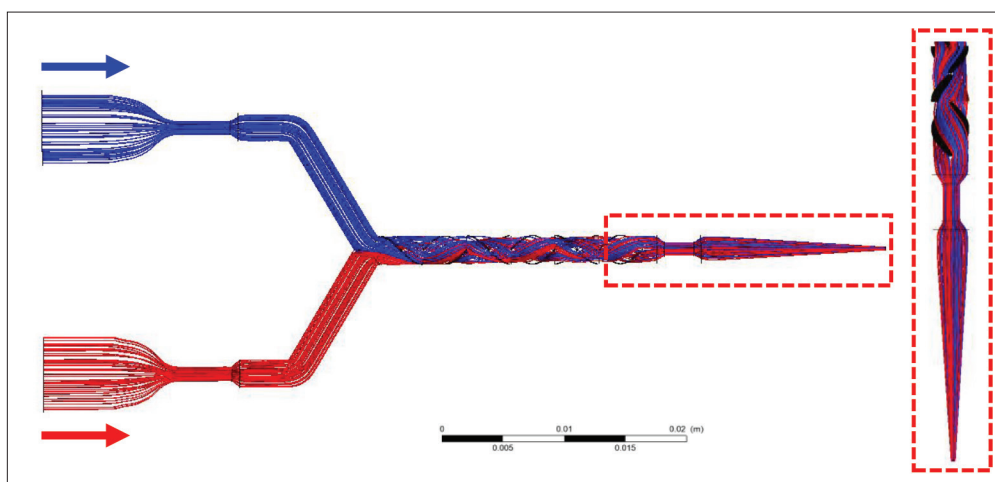
Figure 3. The working principle of the KSM-integrated printing head with conical nozzle. Alginate and gelatin solutions are represented by red- and blue-colored streams, respectively.

where ε indicates the void fraction of the KSM and was set as 0.87.

Another important empirical correlation was proposed by Cybulski and Werdner[54] for $Re<50$:

$$Z = 5.4(1.5) + 0.028Re \qquad (XV)$$

3. Results

3.1. Characterization of material distribution and mixing index

Chaotic advection, also named chaotic stirring, defined as stretching and folding of the fluid layers in a continuous manner, is widely employed in industrial mixing, particularly in the absence of turbulence flow[35,36]. In this case, chaotic advection was achieved by using the Kenics static mixer, which consists of helical mixing units assembled in a cylindrical pipe. CFD simulation was conducted to evaluate the working principle of the KSM system. In this model, each mixing unit of the KSM consecutively divides the incoming flow into two substreams. As the two different material solutions are injected through the printhead, the number of lamellae between them is exponentially increased by each successive mixing elements (Figure 3). The total number of lamellas produced, using n-element KSM, is equal to $s = 2^n$, where s represents the number of mixing units[15]. As the printing head includes six mixing elements, the total number of substreams at the outlet is equal to 32. Additionally, in the case of an uniform distribution of the streams, the thickness of each lamellae can be determined by $d_f/2^n$, where d_f corresponds to the diameter of each lamellae[28]. Then, it is possible to create an internal lamella with adjustable thickness and striation number by changing the number of mixing units in the KSM printing head.

The effect of the number of mixing units on the degree of mixing at different inlet velocities is presented in Figure 4 for the printing head model at different inlet pressures. Results show that the lowest mixing occurs at the cross-sectional plane, where no mixing element is present. As the fluids proceed to the outlet, uniform mass fraction distributions were progressively accomplished, and the mixing index significantly increased. Results also show that once the flow passes the fourth mixing element (near the exit), the mixing index remains almost the same for all considered cases. Similar results have been also reported, suggesting that high mixing quality can be achieved at the fourth or fifth element for nonreactive viscous fluids[55,56]. It is also important to note that the homogeneity of the mixture improves by increasing the extrusion pressure.

3.2. Outlet velocity

The volumetric flux was investigated for both cylindrical and conical nozzle printing heads. To understand the effect of printing pressure and various needle sizes on the flow rate, CFD simulations were conducted, and the results are presented in Figure 5. As observed, the volume flow rate increases by increasing the applied pressure. Moreover, at a constant extrusion pressure, the flow rate is directly proportional to the needle diameter for each nozzle type (Figure 5A and D). In the case of the cylindrical nozzle, the highest flow rate value was 47.75 μL, with a needle diameter of 1.00 mm and an inlet pressure of 3.0 bar, while the lowest flow rate was 0.01 μL with a needle diameter of 0.25 mm and a pressure of 0.5 bar. Additionally, as observed from Figure 5D, the volumetric flow rates are significantly higher in the case of a conical nozzle than in the case of a cylindrical nozzle. At 0.5 bar inlet pressure, for instance, the calculated area-weighted average flow rate in the conical nozzle is nearly 600-fold greater. Results seem
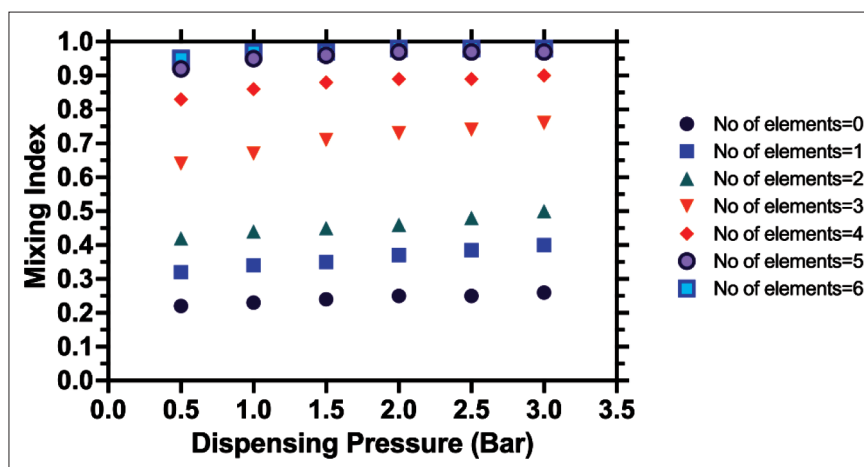
Figure 4. Mixing index results as a function of dispensing pressure for different number of mixing elements.

to indicate that the use of conical needles is the best option, if high volumetric flow rates are required. This is critical if the mixture of hydrogels being dispensed is highly viscous, and inconvenient to distribute with a cylindrical nozzle. It is also important to note that the equivalent flow rates of the printing heads with a cylindrical nozzle can be achieved with substantially lower dispensing pressures in conical nozzle systems. Numerically calculated area-weighted average outlet velocities under various extrusion pressures are presented in Figure 5B and E for cylindrical and conical nozzles.

As the mixture of both polymers moves from the mixing channel to the nozzle, which corresponds to an abrupt change in the cross-sectional area, a significant increase in the linear velocity occurs. Similar to the flow rate results, the velocity magnitude increases at the tip of the nozzles as the applied pressure increases. Results also show that the velocity magnitude reaches a peak value at a pressure of 3 bar and 1 bar for cylindrical and conical nozzles, respectively. It is also important to note that the velocity profile at the nozzle tip is one of the essential parameters, enabling to control the morphology and quality of printed fibers. In Figure 5C and F, the radial distribution of velocity at the nozzle outlet is plotted for different nozzle sizes (ranging from 0.25 to 1.20 mm) and a constant dispensing pressure of 1 bar. As can be observed in Figure 5C, the simulated velocity profiles exhibit a nearly parabolic, fully developed typical Newtonian-like fluid behavior, implying that the shear rates have a lower impact on the mixture viscosity. This can be explained by the low shear rate values, aroused during the deposition process for all considered cases.

The maximum shear rate of 521 s^{-1} was observed for the largest nozzle diameter. These results can be attributed to the power-law index of alginate and gelation

solutions considered in the present study. Since the flow index (n) parameters of each hydrogel forming the mixture are close to 1, which represents a Newtonian fluid, the fluid exhibits a weak shear thinning behavior. However, similar to the results reported by Billiet *et al.* and Ortega *et al.*[34,57], conical nozzle-assembled printing head simulations exhibited higher shear rates. However, contrary to Newtonian fluid's parabolic flow profile, the velocity of the mixing fluid remains almost constant in the center of the nozzle, and rapidly decreases near the walls, where a layer of material mixture undergoes shear thinning (Figure 5F).

This shear-thinned fluid layer behaves as a lubricant, enabling the rest of the intact biomaterial (material at the center) to move through the nozzle in a flow configuration known as plug flow[58]. It is widely accepted that a plug-like flow characteristic might be the mechanism through which the bioinks protect cells from the harmful effects of the high shear stress values[58]. Due to the limited information in terms of flow rate, simulation setup, biomaterial rheology, and printing head geometries, comparison between previous studies is not meaningful. However, it is important to highlight that the flow rate, as a directly shear-determining quantity, is more trustworthy than dispensing pressure, in comparing shear conditions for different nozzle sizes and biomaterials. Figure 5G–L shows velocity distribution maps across the cylindrical and conical nozzles with different outlet diameters (0.25, 0.61, 1.00, and 1.20 mm) for the same applied pressure of 1 bar. As expected, the maximum velocity magnitudes were observed at the center of the nozzle tips. Since no-slip boundary conditions were applied between the biomaterial solution mixture and the walls, a radial velocity gradient was achieved from the walls to the center of the nozzle tip. According to the simulation results, minimum velocity
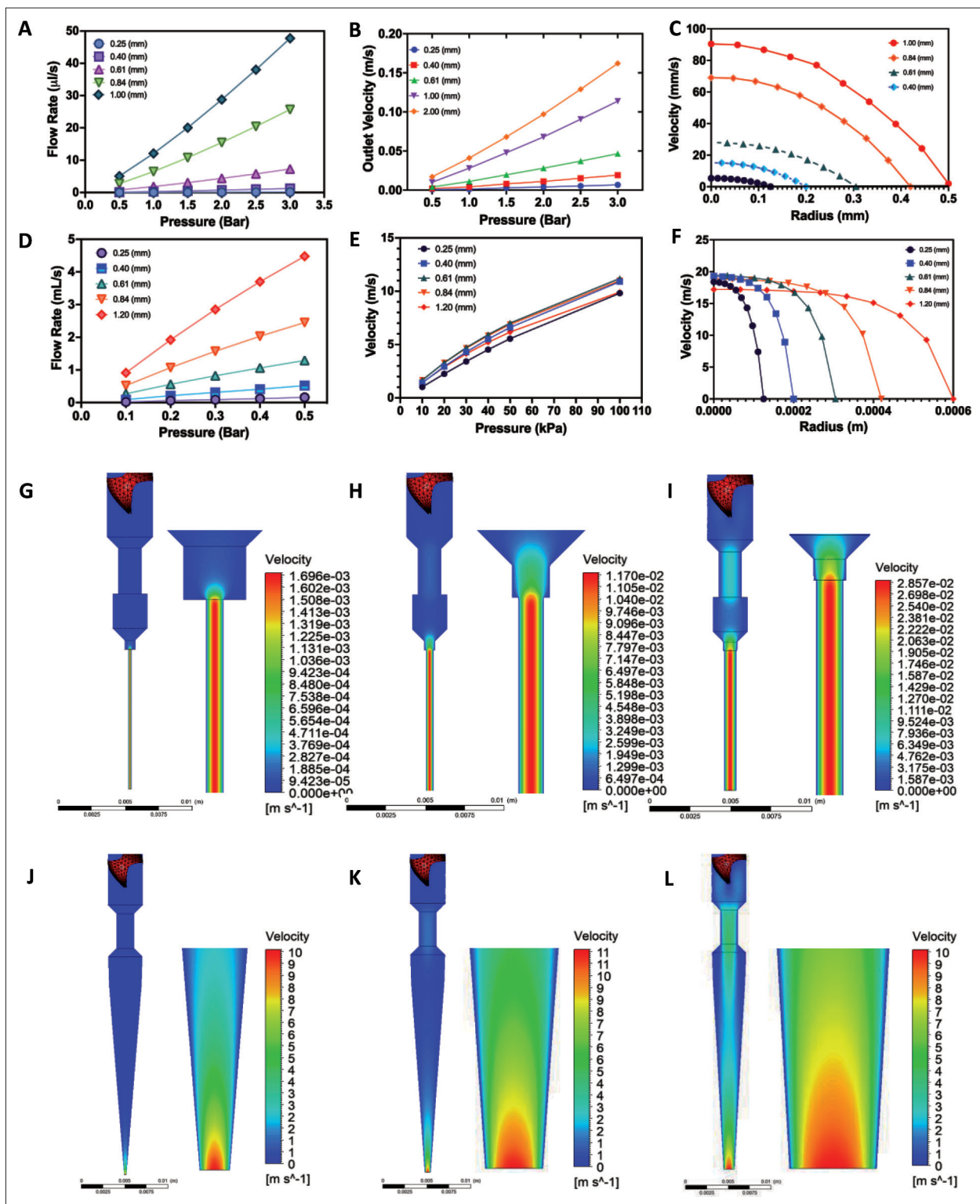
Figure 5. Simulation results for two types of printing needles. Cylindrical nozzle: (A) volumetric flow rate at the nozzle tip versus dispensing pressure, (B) area-weighted outlet average velocity, and (C) velocity profiles across the radius. Conical nozzle: (D) flow rate versus applied pressure, (E) area-weighted outlet average velocity under varying inlet pressures, and (F) the radial velocity distribution for various nozzle sizes. (G, H, I) Cylindrical and (J, K, L) conical nozzle velocity contour plots at 1 bar inlet pressure and different outlet diameters: (G, J) 0.25mm, (H, K) 0.61mm, (I) 1.00mm, and (L) 1.20mm for conical needle.
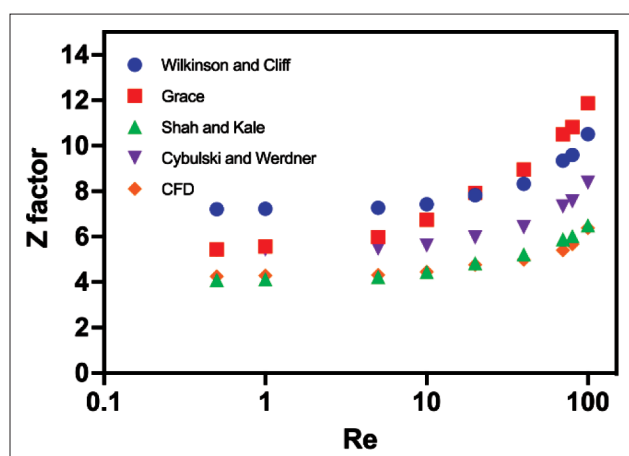
Figure 6. Comparison between simulation results and results obtained from empirical correlations at various *Re* numbers.

values were obtained for the nozzles with smaller diameters, which are aligned with previous reported results[57,59].

3.3. Model validation and pressure drop
To validate the simulation results, the pressure drop values for different *Re* numbers ranging from 0.1 to 100 were compared with empirical correlations, as shown in Figure 6. As observed for the creeping flow (*Re* < 10), the *Z*-factor remains almost constant for the KSM. However, as the *Re* rises, an increment was observed in the *Z* values. Results from Figure 6 suggest that higher Reynolds numbers result in higher pressure drop. Moreover, our CFD results are well aligned with the results predicted by Equation XIV, for a given range of *Re* numbers. Based on the findings of Meng *et al.*[60], the Z-factor of a Kenics static mixer with an aspect ratio of 1.5 ranges from 5.64 to 8.63.

Previous studies investigating the deposition process only focused on the pressure drop inside the printing nozzle, without taking the barrels into account[30,54-55]. In this study, the pressure drop was comprehensively analyzed along the entire extrusion printing head, including barrels, KSM, and needles with different types and outlet diameters. As shown in Figure 7A and B, the pressure drop in the mixing chamber is negligible, as the inner diameter of the KSM is relatively larger than the nozzle diameters. For a dispensing pressure of 1 bar, the highest pressure drop occurred in the narrowing part of the printing head for all conical nozzle diameters (0.25, 0.40, 0.61, 0.84, and 1.00 mm) (Figure 7B and C). Moreover, as the mixture of the two polymeric solutions passes from the static mixer to the cylindrical needle, a significant pressure drop was observed regardless of the needle length (Figure 7D and E). hese results suggest that using finer nozzles will cause higher pressure drops, compared to nozzles with larger inner diameters. This can be attributed to the energy loss, caused by the wall-channel-

related hydrodynamic resistance against the material flow, which requires higher dispensing pressures. Applying high pressures at the inlets can have a detrimental impact on the cell viability, also requiring the use of systems with more powerful pumps[28]. Nair *et al.*[61] also observed that the use of a nozzle tip, with a diameter of 0.15 mm and high extrusion pressure (40 psi≈ 2.75 bar), resulted in karyolysis as well as pyknosis.

3.4. Shear stress
The level of shear stress was carefully investigated in terms of key printing parameters, such as nozzle type, dispensing pressure, and needle diameter. Since the simulations were conducted for the entire printing head, the shear stress condition in the mixing chamber was first determined (Figure 8A). The simulation results showed that using the Kenics static mixer inside the printing head does not lead to a dramatic increase in the shear stress, as previously reported[28]. The shear stress distribution was further investigated for the cylindrical and conical nozzles at various dispensing pressures, and the results are presented in Figure 8B and C. As expected, results show that the nozzle is the most critical component of the entire printing system. This is mainly due to the abrupt narrowing of the cross-section in the nozzle domain, which results in a significant increase in the velocity field.

The shear stress inside the flow domain is generated by the velocity gradient[62-64]. Simulation results revealed that the maximum shear stress occurs at the needle walls, being minimum along the central axis for both needle types. Moreover, as observed from Figure 8B–E, for the same inlet pressure values, the highest shear stresses occur for the cone-shaped nozzle type (≈6 kPa). However, this is only visible at the very tip of the nozzle. On the other hand, the use of a cylindrical nozzle generates lower shear stresses along the nozzle length (≈1 kPa), but for a higher passage length (12 mm). Figure 8C depicts shear stress curves as a function of extrusion pressure for different conical nozzle diameters. The obtained results are similar to those obtained by Billiet *et al.*[34], who investigated the cell viability of HepG2 cells using different needle types. They carried out a finite element modeling simulation considering non-crosslinked cell-gelatin methacrylamide as the working fluid, and obtained higher peak shear stresses at 1 bar extrusion pressures for the conical nozzle in comparison with the cylindrical nozzle setup. Our results for conical shaped nozzle are also in a good agreement with reported studies by Emmermacher *et al.*[1] and Samandari *et al.*[28]. Figure 8D shows that, by reducing the needle outlet diameter or by increasing the dispensing pressure, the shear stress at the needle walls increases. However, these findings do not coincide with those from Liu *et al.*[65],
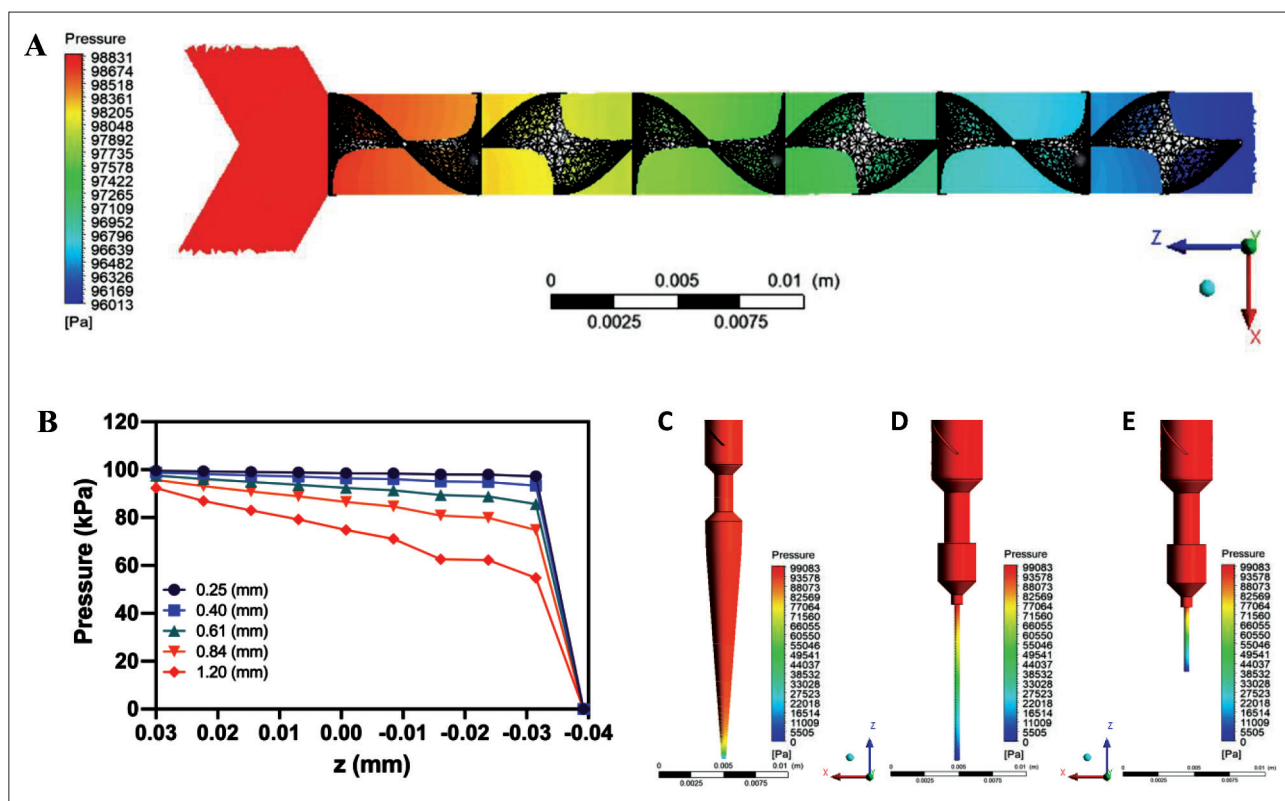
Figure 7. Pressure drop results for an inlet pressure of 1 bar. (A) The local pressure contour plot in the mixing chamber. (B) Variation of pressure along the axial direction of the printing head; contour plots of pressure drop for different nozzle types with outlet diameter of 0.4 mm. (C) Conical needle, (D) long cylindrical needle (12 mm), and (E) short cylindrical needle (5 mm).

as we obtained higher stress values for the conical nozzle type, which can be attributed to the different boundary conditions anddifferent bioink used in the simulations. Muller *et al.*[32] also investigated shear stresses for alginate/sulfate nanocellulose bioink through 2D axisymmetric finite element fluid flow simulations. They investigated the effect of shear stress using different nozzle types with varying outlet diameters. However, similar to Liu *et al.*[65], their findings cannot be directly compared with those from our study due to the different printing head geometry, applied biomaterials and boundary conditions.

In the case of cylindrical nozzles, shear stress distribution profiles at different inlet pressures (1, 2, and 3 bar) over the radius of nozzle outlet diameters ranging from 0.25 mm to 1.00 mm are illustrated in Figure 9. Results show that the shear stress distribution along the radial direction is linear, and it is nearly zero in the channel core. In addition, increasing the applied inlet pressure from 1 to 3 bar resulted in higher shear values, for all investigated nozzle diameters and shapes, which is aligned with other reported studies[32,33]. In all considered cases, the magnitude of the shear stress at the needle walls ranges between 0.5 and 4.8 kPa. The highest shear stress

was obtained when a needle radius of 1.00 mm and 3 bar inlet pressure were employed, whereas the lowest stress occurred in the smallest cylindrical needle flow (0.25 mm) at 1 bar extrusion pressure.

These results seem to suggest that conically shaped needles are favored over straight needle types when the inlet pressure dependency is low, but this tends to disappear at greater dispensing pressures. We anticipate that at lower pressures, which correspond to longer passage time, the enhanced passage of high shear stress for the straight nozzle will have a greater impact on the cells. However, at higher extrusion pressures, the induced shear stress will be dramatically higher, and the lower passage time for the conical nozzle will no longer be able to compensate these high shear magnitudes. In their cell survival studies, Billiet *et al.*[34] showed that the conical nozzle exhibit high cell viability levels (>97% at low inlet pressures of <1 bar), but higher dispensing pressures resulted in substantial viability loss when compared to the straight nozzle type. Recently, Blaeser *et al.*[66] showed that for shear stress magnitudes below 5 kPa, the cell viability was almost not affected by the deposition process. The average cell viability was also examined for applied shear
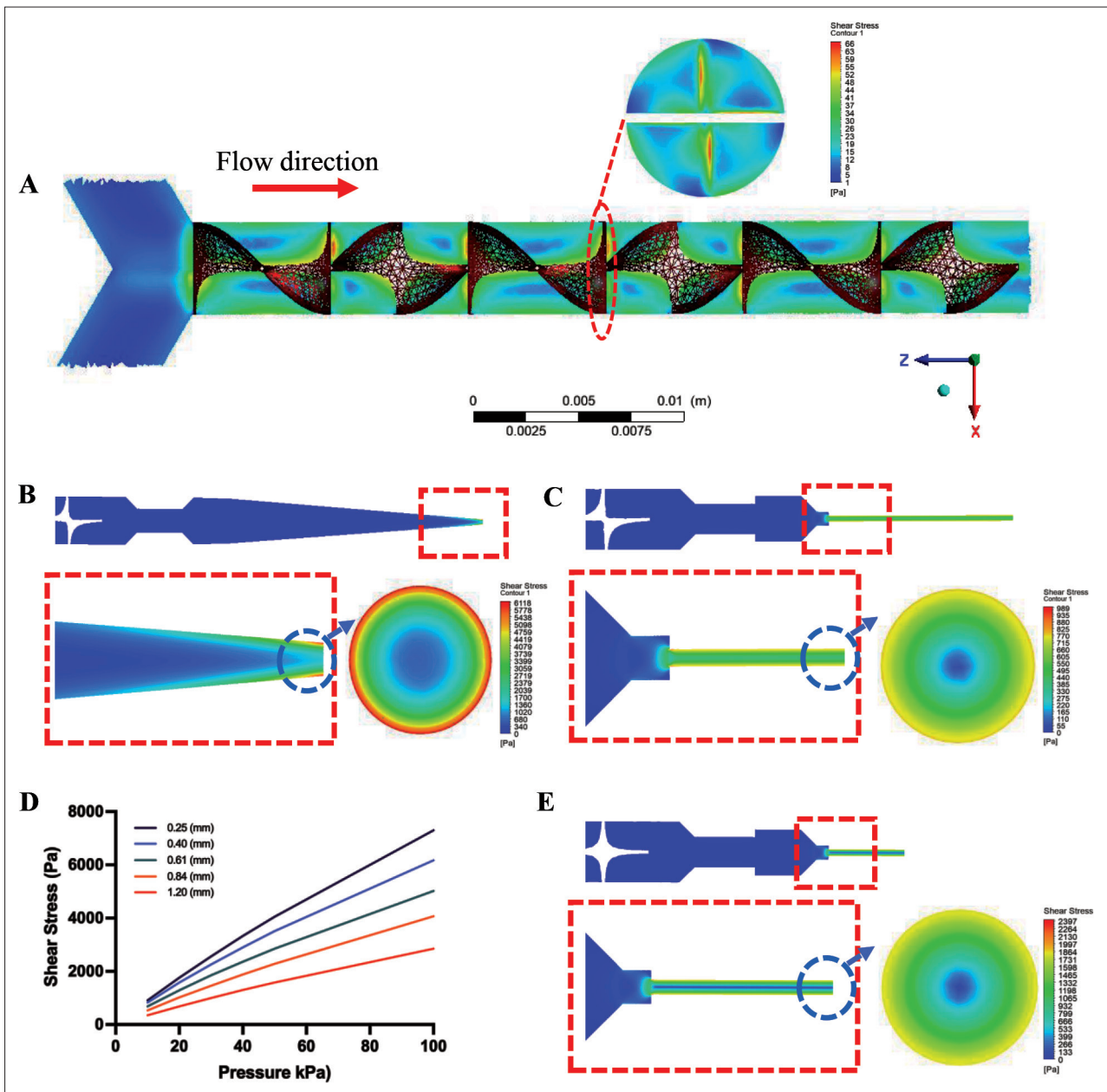
Figure 8. Shear stress distribution results for 1 bar of dispensing pressure. (A) Heat map of the shear stress along the KSM-inserted mixing channel. (B) Conical nozzle with a diameter of 0.4 mm.(C) Long cylindrical nozzle (12mm) with 0.4 mm outlet diameter.(D) Variation of shear stress as a function of applied pressure and nozzle diameter. (E)Contour plot of shear stress for short needle (5 mm).

stresses in the range of 5–10 kPa and >10kPa. Results revealed that the viability of cells decreased from 96% to 91% for moderate shear stresses (5–10 kPa), whereas a significant decrease was observed for the shear stresses over 10 kPa (76% of cell viability). Based on our simulation results, the maximum shear stress observed in the mixing channel was around 66 Pa. The highest shear stress for straight nozzles was below 5 kPa in all cases, whereas the peak stress values were obtained for conical

needles with small outlet diameters (0.25 and 0.40 mm) at applied pressures of 1 bar. These results suggest that our printing heads will induce negligible cell damage. It should be noted that the rheological data, considered in our CFD simulations, was related to alginate and gelatin solutions without cells. However, several results demonstrated that, even in the case of high cell densities, no significant changes were observed on the bioink rheological characteristics[1,31,66,67].
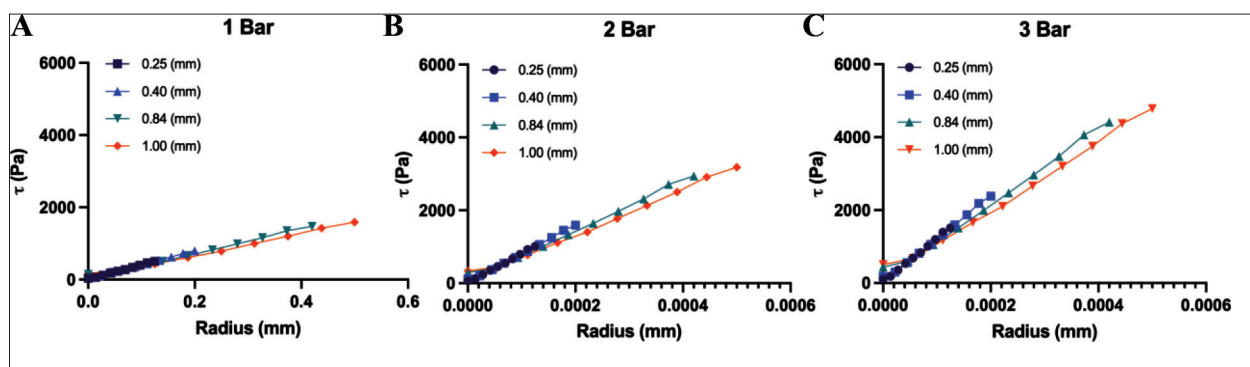
Figure 9. Shear stress profiles as a function of the cylindrical nozzle outlet radius at different inlet pressures. (A) 1 bar, (B) 2 bar, and (C) 3 bar.

4. Conclusion

The CFD model presented in this study enables to investigate the fluid flow of two different biopolymers in a KSM-integrated printing head during the extrusion process. The volumetric flow rate, pressure gradient, shear-thinning behavior of the alginate–gelatin mixture, and the shear stress that occurs in the fluid domain were successfully predicted using numerical results, allowing to optimize the bioprinting process and to reduce the laborious trial-and-error experimental approach. The spatial distribution of the biomaterials was analyzed at each successive cross-sectional planes along the mixing chamber. Due to the presence of chaotic advection, the proposed printhead exhibited high mixing performance, regardless of the applied pressure from the inlets. The volumetric flow rate and velocity field were deeply investigated for cylindrical and conical shaped nozzles, with different diameters under varying dispensing pressures. Results suggest that, if high bioprinting velocities are required, conical nozzles seem to be the most suitable option. It was also observed that the obtained maximum shear stress values were sufficiently low to sustain high cellular viability.

Future work will focus on the extrusion of multimaterials in the printing platform using a numerical model to further investigate operating parameters, such as the nozzle tip-build plate distance, relative velocity between nozzle and substrate, and morphological analysis of the fibers after the deposition process.

Conflict of interest

The authors declare no conflict of interest. The funders had no role in the design of the study; in the collection, analyses, or interpretation of data; in the writing of the manuscript; or in the decision to publish the results.

Author contributions

Conceptualization: Paulo Bartolo
Investigation: Gokhan Ates
Methodology: Gokhan Ates
Writing – original draft: Gokhan Ates
Writing – review & editing: Paulo Bartolo

Ethics approval and consent to participate

Not applicable.

Consent for publication

Not applicable.

Availability of data

Data can be provided by request.

References

1. Emmermacher J, Spura D, Cziommer J, *et al.*, 2020, Engineering considerations on extrusion-based bioprinting: Interactions of material behavior, mechanical forces and cells in the printing needle. *Biofabrication*, 12(2):2–16.

   https://doi.org/10.1088/1758-5090/ab7553

2. Jiang T, Munguia-Lopez JG, Flores-Torres S, *et al.,* 2019, Extrusion bioprinting of soft materials: An emerging technique for biological model fabrication. *Appl Phys Rev*, 6(1).

   https://doi.org/10.1063/1.5059393

3. Trujillo-De Santiago G, Alvarez M, Samandari M, *et al.*, 2018, Chaotic printing: Using chaos to fabricate densely packed micro- and nanostructures at high resolution and speed. *Mater Horizons*, 5(5):813–822.

https://doi.org/10.1039/c8mh00344k

4. Gungor-Ozkerim PS, Inci I, Zhang YS, *et al.*, 2018, Bioinks for 3D bioprinting: An overview. *Biomater Sci*, 6(6):915–946.

https://doi.org/10.1039/c7bm00765e

5. Bartolo P, Malshe A, Ferraris E, *et al.*, 2022, 3D bioprinting: Materials, processes, and applications. *CIRP Ann*, 71(2): 577–597.

https://doi.org/10.1016/j.cirp.2022.06.001

6. Liu F, Vyas C, Yang J, *et al.,* 2021, A review of hybrid biomanufacturing systems applied in tissue regeneration, in *Virtual Prototyping & Bio Manufacturing in Medical Applications*, 187–213.

https://doi.org/10.1007/978-3-030-35880-8_8

7. Li X, Liu B, Pei B, *et al.,* 2020, Inkjet bioprinting of biomaterials. *Chem Rev*, 120(19):10793–10833.

https://doi.org/10.1021/acs.chemrev.0c00008

8. Ng WL, Xi H, Shkolnikov V, *et al.*, 2021, Controlling droplet impact velocity and droplet volume: Key factors to achieving high cell viability in sub-nonoliter droplet-based bioprinting. *Int J Bioprint*, 8(1):424.

https://doi.org/10.18063/IJB.V8I1.424

9. Zhuang P, Ng WL, An J, *et al.*, 2019, Layer-by-layer ultraviolet assisted extrusion-based (UAE) bioprinting of hydrogel constructs with high aspect ratio for soft tissue engineering applications. *PLoS One*, 14(6):e0216776.

https://doi.org/10.1371/journal.pone.0216776

10. Ng WL, Lee JM, Zhou M, *et al.*, 2020, Vat polymerization-based bioprinting-process, materials, applications and regulatory challenges. *Biofabrication*, 12(2):022001.

https://doi.org/10.1088/1758-5090/ab6034

11. Li W, Mille LS, Robledo JA, *et al.*, 2020, Recent advances in formulating and processing biomaterial inks for vat polymerization-based 3D printing. *Adv Healthc Mater*, 9(15):e2000156.

https://doi.org/10.1002/adhm.202000156

12. Ning L, Chen X, 2017, A brief review of extrusion-based tissue scaffold bio-printing. *Biotechnol J*, 12(8).

https://doi.org/10.1002/biot.201600671

13. Ozbolat IT, Hospodiuk M, 2016, Current advances and future perspectives in extrusion-based bioprinting. *Biomaterials*, 76:321–343.

https://doi.org/10.1016/j.biomaterials.2015.10.076

14. Kang D, Hong G, An S, *et al.*, 2020, Bioprinting of multiscaled hepatic lobules within a highly vascularized construct. *Small*, 16(13):1–9.

https://doi.org/10.1002/smll.201905505

15. Chávez-Madero C, Derby MD, Samandari M, *et al.*, 2020, Using chaotic advection for facile high-throughput fabrication of ordered multilayer micro-and nanostructures: Continuous chaotic printing. *Biofabrication*, 12(3).

https://doi.org/10.1088/1758-5090/ab84cc

16. Ravanbakhsh H, Karamzadeh V, Bao G, *et al.,* 2021, Emerging technologies in multi-material bioprinting. *Adv Mater*, 33(49).

https://doi.org/10.1002/adma.202104730

17. Costantini M, Testa S, Mozetic P, *et al.*, 2017, Microfluidic-enhanced 3D bioprinting of aligned myoblast-laden hydrogels leads to functionally organized myofibers in vitro and in vivo. *Biomaterials*, 131:98–110.

https://doi.org/10.1016/j.biomaterials.2017.03.026

18. Prendergast ME, Burdick JA, 2020, Recent advances in enabling technologies in 3D printing for precision medicine. *Adv Mater*, 32(13).

https://doi.org/10.1002/adma.201902516

19. Sodupe-Ortega E, Sanz-Garcia A, Pernia-Espinoza A, *et al.*, 2018, Accurate calibration in multi-material 3D bioprinting for tissue engineering. *Materials (Basel)*, 11(8):1–19.

https://doi.org/10.3390/ma11081402

20. Kolesky DB, Truby RL, Gladman AS, *et al.,*2014, 3D bioprinting of vascularized, heterogeneous cell-laden tissue constructs. *Adv Mater*, 26(19):3124–3130.

https://doi.org/10.1002/adma.201305506

21. Nadernezhad A, Khani N, Skvortsov G, *et al.*, 2016, Multifunctional 3D printing of heterogeneous hydrogel structures. *Sci Rep*, 6.

https://doi.org/10.1038/srep33178

22. Liu W, Zhang YS, Heinrich MA, *et al.*, 2017, Rapid continuous multimaterial extrusion bioprinting. *Adv Mater*, 29(3):1–8.

https://doi.org/10.1002/adma.201604630

23. Colosi C, Shin SR, Manoharan V, *et al.*, 2016, Microfluidic bioprinting of heterogeneous 3D tissue constructs using low-viscosity bioink. *Adv Mater*, 28(4):677–684a.

https://doi.org/10.3390/MI11050459

24. Wang J, Zhang N, Chen J, *et al.,* 2019, Finding the optimal design of a passive microfluidic mixer. *Lab Chip*, 19(21):3618–3627.

https://doi.org/10.1039/c9lc00546c

25. Ceballos-González CF, Bolívar-Monsalve EJ, Quevedo-Moreno DA, *et al.*, 2021, High-throughput and continuous chaotic bioprinting of spatially controlled bacterial microcosms. *ACS Biomater Sci Eng*, 7(6):2408–2419.

https://doi.org/10.1021/acsbiomaterials.0c01646

26. Li M, Tian X, Schreyer DJ, *et al.,* 2011, Effect of needle geometry on flow rate and cell damage in the dispensing-based biofabrication process. *Biotechnol Prog*, 27(6):1777–1784.

https://doi.org/10.1002/btpr.679

27. Andrew CD, Susan EC, Emily MR., *et al.*, 2016, A comparison of different bioinks for 3D bioprinting of fibrocartilage and hyaline cartilage. *Biofabrication*, 8(4):45002.

https://doi.org/10.1088/1758-5090/8/4/045002

28. Samandari M, Alipanah F, Majidzadeh AK, *et al.,* 2021, Controlling cellular organization in bioprinting thrountalizationgh designed 3D microcompartme. *Appl Phys Rev*, 8(2).

https://doi.org/10.1063/5.0040732

29. Yu Y, Zhang Y, Martin JA, *et al.,* 2013, Evaluation of cell viability and functionality in vessel-like bioprintable cell-laden tubular channels. *J Biomech Eng*, 135(9):1–9.

https://doi.org/10.1115/1.4024575

30. Li M, Tian X, Zhu N, 2010, Modeling process-induced cell damagein the biodispensing process. *Tissue Eng Part C: Methods*, 16(3):533–542.

https://doi.org/10.1089=ten.tec.2009.0178533

31. Chiesa I, Ligorio C, Bonatti AF, *et al.*, 2020, Modeling the three-dimensional bioprinting process of β-sheet self-assembling peptide hydrogel scaffolds. *Front Med Technol*, 2:1–16.

https://doi.org/10.3389/fmedt.2020.571626

32. Müller M, Öztürk E, Arlov Ø, *et al.,* 2017, Alginate sulfate–nanocellulose bioinks for cartilage bioprinting applications. *Ann Biomed Eng*, 45(1):210–223.

https://doi.org/10.1007/s10439-016-1704-5

33. Serna JA, Florez SL, Talero VA, *et al.,* 2019, Formulation and characterization of a SIS-based photocrosslinkable bioink. *Polymers (Basel)*, 11(3):1–10.

https://doi.org/10.3390/polym11030569

34. Billiet T, Gevaert E, De Schryver T, *et al.,* 2014, The 3D printing of gelatin methacrylamide cell-laden tissue-engineered constructs with high cell viability. *Biomaterials*, 35(1):49–62.

https://doi.org/10.1016/j.biomaterials.2013.09.078

35. Mahammedi A, Ameur H, Ariss A, *et al.,* 2017, Numerical investigation of the performance of Kenics static mixers for the agitation of shear thinning fluids. *J Appl Fluid Mech*, 10(3):989–999.

https://doi.org/10.18869/acadpub.jafm.73.240.27314

36. Hobbs DM, Swanson PD, Muzzio FJ, 1998, Numerical characterization of low Reynolds number flow in the Kenics static mixer. *Chem Eng Sci*, 53(8):1565–1584.

https://doi.org/10.1016/S0009-2509(97)00132-2

37. Nyande BW, Mathew Thomas K, Lakerveld R, 2021, CFD analysis of a Kenics static mixer with a low pressure drop under laminar flow conditions. *Ind Eng Chem Res*, 60(14):5264–5277.

https://doi.org/10.1021/acs.iecr.1c00135

38. Bird RB, 2007, Transport Phenomena Rev, 2nd ed, New York, Wiley.

39. Chhabra RP, Richardson JF, 2011, Chapter 1. Non-Newtonian fluid behaviour, in *Non-Newtonian Flow and Applied Rheology: Engineering Applications*, 536.

https://doi.org/10.1016/b978-075063770-1/50002-6

40. Neofytou P, 2005, A 3rd order upwind finite volume method for generalised Newtonian fluid flows. *Adv Eng Softw*, 36(10):664–680.

https://doi.org/10.1016/j.advengsoft.2005.03.011

41. Metzner AB, 1957, Non-Newtonian fluid flow relationships between recent pressure-drop correlations. *Ind Eng Chem*, 49(9):1429–1432.

https://doi.org/10.1021/ie50573a049

42. Blaeser A, Million N, Campos DFD, *et al.*, 2016, Laser-based in situ embedding of metal nanoparticles into bioextruded alginate hydrogel tubes enhances human endothelial cell adhesion. *Nano Res*, 9(11):3407–3427.

https://doi.org/10.1007/s12274-016-1218-3

43. Thompson JF, Soni BK, Weatherill NP, 1999, *Handbook of Grid Generation*, Boca Raton, FL, CRC Press.

https://doi.org/10.1201/9781420050349

44. Thakur RK, Vial C, Nigam KDP, *et al.,* 2003, Static mixers in the process industries—A review, 81.

https://doi.org/10.1205/026387603322302968

45. Rafeie M, Welleweerd M, Hassanzadeh-Barforoushi A, *et al.,* 2017, An easily fabricated three-dimensional threaded lemniscate-shaped micromixer for a wide range of flow rates. *Biomicrofluidics*, 11(1).

https://doi.org/10.1063/1.4974904

46. Santana HS, Silva JL, Taranto OP, 2015, Numerical simulation of mixing and reaction of Jatropha curcas oil and ethanol for synthesis of biodiesel in micromixers. *Chem Eng Sci*, 132:59–168.

https://doi.org/10.1016/j.ces.2015.04.014

47. Zhang J, Luo X, 2018, Mixing performance of a 3D micro T-mixer with swirl-inducing inlets and rectangular constriction. *Micromachines*, 9(5).

https://doi.org/10.3390/mi9050199

48. Shah I, Kim SW, Kim K, *et al.,* 2019, Experimental and numerical analysis of Y-shaped split and recombination micro-mixer with different mixing units. *Chem Eng J*, 358:691–706.

    https://doi.org/10.1016/j.cej.2018.09.045

49. Raza W, Hossain S, Kim KY, 2017, Effective mixing in a short serpentine split-and-recombination micromixer. *Sensors Actuators B Chem*, 258:381–392.

    https://dx.doi.org/10.1016/j.snb.2017.11.135

50. Mouheb NA, Malsch D, Montillet A, *et al.,* 2012, Numerical and experimental investigations of mixing in T-shaped and cross-shaped micromixers. *Chem Eng Sci*, 68(1):278–289.

    https://doi.org/10.1016/j.ces.2011.09.036

51. Rauline D, Tanguy PA, Le Blévec JM, *et al.*, 1998, Numerical investigation of the performance of several static mixers. *The Canadian J Chem Eng*, 76(3):527–535.

    https://doi.org/10.1002/cjce.5450760325

52. Grace HP, 1982, Dispersion phenomena in high viscosity immiscible fluid systems and application of static mixers as dispersion devices in such systems. *Chem Eng Commun*, 14(3–6):225–277.

    https://doi.org/10.1080/00986448208911047

53. Shah NF, Kale DD, 1991, Pressure drop for laminar flow of non-Newtonian fluids in static mixers. *Chem Eng Sci*, 46(8):2159–2161.

    https://doi.org/10.1016/0009-2509(91)80175-X

54. Haddadi MM, Hosseini SH, Rashtchian D, *et al.,* 2020, Comparative analysis of different static mixers performance by CFD technique: An innovative mixer. *Chin J Chem Eng*, 28(3):672–684.

    https://doi.org/10.1016/j.cjche.2019.09.004

55. Ates G, Bartolo P, 2021, Numerical simulation of multimaterial polymer mixing for bioprinting applications. *J Addit Manuf Technol*, 1(3):606.

    https://10.18416/JAMTECH.2111606

56. Hozumi T, Ohta S, Ito T, 2015, Analysis of the calcium alginate gelation process using a Kenics static mixer. *Ind Eng Chem Res*, 54(7):2099–2107.

    https://doi.org/10.1021/ie5044693

57. Ortega ES, Sanz-Garcia A, Pernia-Espinoza A, *et al.*, 2019, Efficient fabrication of polycaprolactone scaffolds for printing hybrid tissue-engineered constructs. *Materials (Basel)*, 12(4):1–18.

    https://doi.org/10.3390/ma12040613

58. Aguado BA, Mulyasasmita W, Su J, *et al.,* 2012, Improving viability of stem cells during syringe needle flow through the design of hydrogel cell carriers. *Tissue Eng Part A*, 18(7-8):806–815.

    https://doi.org/10.1089/ten.tea.2011.0391

59. Gómez-Blanco JC, Mancha-Sánchez E, Marcos AC, *et al.,* 2020, Bioink temperature influence on shear stress, pressure and velocity using computational simulation. *Processes*, 8(7):1–18.

    https://doi.org/10.3390/PR8070865

60. Meng HB, Song MY, Yu YF, *et al.,* 2017, Enhancement of laminar flow and mixing performance in a lightnin static mixer. *Int J Chem React Eng*, 15(3):1–21.

    https://doi.org/10.1515/ijcre-2016-0112

61. Nair K, Gandhi M, Khalil S, *et al.*, 2009, Characterization of cell viability during bioprinting processes. *Biotechnol J*, 4(8):1168–1177.

    https://doi.org/10.1002/biot.200900004

62. Sarker M, Chen XB, 2017, Modeling the flow behavior and flow rate of medium viscosity alginate for scaffold fabrication with a three-dimensional bioplotter. *J Manuf Sci Eng Trans ASME*, 139(8):1–14.

    https://doi.org/10.1115/1.4036226

63. Paxton N, Smolan W, Böck T, *et al.,* 2017, Proposal to assess printability of bioinks for extrusion-based bioprinting and evaluation of rheological properties governing bioprintability. *Biofabrication*, 9(4).

    https://doi.org/10.1088/1758-5090/aa8dd8

64. Snyder J, Son AR, Hamid Q, et al., 2015, Mesenchymal stem cell printing and process regulated cell properties. *Biofabrication*, 7(4).

    https://doi.org/10.1088/1758-5090/7/4/044106

65. Liu W, Heinrich MA, Zhou Y, *et al.*, 2017, Extrusion bioprinting of shear-thinning gelatin methacryloyl bioinks. *Adv Healthc Mater*, 6(12):1–11.

    https://doi.org/10.1002/adhm.201601451

66. Blaeser A, Campos DFD, Puster U, *et al.,* 2016, Controlling shear stress in 3D bioprinting is a key factor to balance printing resolution and stem cell integrity. *Adv Healthc Mater*, 5(3):326–333.

    https://doi.org/10.1002/adhm.201500677

67. Manojlovic V, Djonlagic J, Obradovic B, *et al.,* 2006, Investigations of cell immobilization in alginate: Rheological and electrostatic extrusion studies. *J Chem Technol Biotechnol*, 81(4):505–510.

    https://doi.org/10.1002/jctb.1465